

Chapter 6

A Pariser–Parr–Pople Model Hamiltonian-Based Approach to the Electronic Structure and Optical Properties of Graphene Nanostructures

Kondayya Gundra and Alok Shukla

Abstract The electronic structure of graphene and related nanostructures such as graphene nanoribbons and quantum dots is frequently described within the π -electron approaches such as the tight-binding model, which completely ignores the electron–electron interactions, or the Hubbard model which takes into account only the on-site part. In theoretical chemistry, Pariser–Parr–Pople (PPP) model Hamiltonian, which takes into account the long-range part of the inter-electron Coulomb interaction, has been employed extensively, and with considerable success, to study the electronic structure and optical properties of π -conjugated molecules and polymers. Therefore, with the aim of exploring the influence of long-range Coulomb interactions on the electronic structure and optical properties of graphene nanostructures, we have recently developed a numerical approach based upon the PPP model Hamiltonian and used it to study their band structure, magnetic order, and the linear optical absorption spectra. In this chapter, we describe our approach in detail and present its numerous applications ranging from finite systems such as fullerene C₆₀ and graphene quantum dots to infinitely long quasi-one-dimensional graphene nanoribbons. Our approach is computationally inexpensive and yields results in good agreement with the large-scale first-principles calculations reported by other authors. Furthermore, some of the novel predictions resulting from our approach are also discussed.

K. Gundra

Theoretical Physics Division, Bhabha Atomic Research Centre, Mumbai 400085, India

Department of Physics, Indian Institute of Technology, Bombay, Powai, Mumbai 400076, India

e-mail: naiduk@barc.gov.in

A. Shukla (✉)

Department of Physics, Indian Institute of Technology, Bombay, Powai, Mumbai 400076, India

e-mail: shukla@phy.iitb.ac.in

6.1 Introduction

The electronic structure and optical properties of π -conjugated molecules have attracted both physicists and chemists alike for a long time (Barford 2005; Barieswyl et al. 1992; Salem 1966), because of their potential applications in optoelectronic devices such as light-emitting diodes, field-effect transistors, lasers, and solar cells etc. (Malliaras and Friend 2005). This field received a further boost with the synthesis of molecules like C_{60} (Kroto et al. 1985) and other fullerenes (Andreoni 2000), as also carbon nanotubes (Dresselhaus et al. 2001; Iijima 1991), all of which have tremendous potential for device applications. However, ever since the synthesis of graphene (Novoselov et al. 2004) and its nanostructures such as graphene nanoribbons, and nanodisks, etc. (Geim and Novoselov 2007), interest in the physics of π -electron systems has grown many folds (Neto et al. 2009). These systems exhibit exotic transport and electronic properties, leading to the possibility that in future electronic devices, graphene will be able to replace silicon as the material of first choice (Geim and Novoselov 2007; Neto et al. 2009; Palacios et al. 2010).

For a theoretician, several possible approaches are available which can describe the electronic structure of graphene and related nanostructures, as well as other π -conjugated systems: (a) fully first-principles approaches based upon the mean-field methods such as the density-functional theory (DFT) (Barone et al. 2006; Prezzi et al. 2008; Son et al. 2006a; Yang et al. 2007a,b, 2008) or the Hartree-Fock (HF) method (Kertesz 1982; Pisani and Dovesi 1980; Shukla et al. 1996, 1999, 1998), (b) methods based upon effective π -electron models such as the one-particle tight-binding (TB) theory (Ezawa 2006; Fujita et al. 1996; Nakada et al. 1996) and its electron-correlated extensions such as the Hubbard (Jung and MacDonald 2009; Voronov 2007; Yazyev 2008) or the extended Hubbard model (Yamashiro et al. 2003), and (c) Dirac-equation-based massless Fermion approach (Neto et al. 2009). The first-principles methods are normally computationally quite expensive because they treat all electrons (except the core electrons) explicitly and therefore require the use of large basis sets to provide a reasonable description of the electronic structure of such systems. In case of graphene nanoribbons (GNRs) of large widths, large graphene nanoflakes, and also polymers with big unit cells, the number of degrees of freedom involved in the problem may impose severe computational constraints on the problems which can be tackled.

The Dirac-equation-based massless Fermion approach to the graphene and its nanostructures is quite popular among theoreticians at present (Neto et al. 2009). It is derived from the TB model for graphene under the effective mass approximation and is based upon the linearity of the band structure with respect to the \mathbf{k} vector in the vicinity of the so-called Dirac points (Neto et al. 2009). Therefore, its validity is restricted to a small region of the Brillouin zone (BZ) near the Dirac points, and it is far less justified to use it for the reduced-dimensional graphene structures such as the nanoflakes and the nanoribbons.

Compared to the first-principles approaches, effective π -electron models offer an attractive alternative in that they explicitly deal only with the π electrons, thereby reducing the number of electrons to be taken into account significantly, and, thus allowing one to simulate systems of much larger sizes. In such models, the effect of σ -electrons is included in an implicit manner in terms of various parameters of the Hamiltonian such as the hopping matrix elements. Furthermore, they can be used both for finite and infinite systems. In particular, for infinite periodic systems, their range of validity extends over the entire BZ, unlike the Dirac-equation-based approaches, which are applicable only in the neighborhood of the Dirac points. The disadvantage of such approaches is their semiempirical nature, implying the presence of parameters in the model which are determined by means other than the first principles. However, when materials with a large number of atoms need to be studied, first-principles approaches are computationally often not feasible. For such systems model Hamiltonians are sometimes the only possible options. The fact that such models are extremely popular in physics even for smaller systems, testifies to the insights they offer into the electronic structure of such materials, irrespective of their size.

Among the semiempirical methods employed most commonly in the studies of π -conjugated systems, the TB model (called the Hückel model in the chemistry literature) is conceptually the simplest, but it does not include the effects of electron–electron (e–e) interactions. One can correct that deficiency by employing the Hubbard model or its extended versions which include the on-site and the nearest-neighbor Coulomb interactions, respectively. However, it is well known in the chemistry literature that in π -electron systems such as aromatic molecules and conjugated polymers, the long-range part of the e–e interactions plays a very important role in determining their electronic structure (Barford 2005; Barieswyl et al. 1992; Salem 1966). In the 1950s, Pariser, Parr, and Pople proposed a conceptually simple model which incorporates the essential physics of interacting π -electron systems in an elegant manner (Pariser and Parr 1953) and has come to be known as the PPP model since then. This model can also be seen as an extension of the Hubbard model in that, in addition to the on-site repulsion (Hubbard U), long range e–e interactions are taken into account by means of suitable Coulomb parameters. Unlike the extended Hubbard models the PPP model imposes no restrictions on the range of Coulomb interactions, thereby leading to the inclusion of interactions between all the sites, irrespective of the distance between them. Because the PPP model is also a π -electron model, the number of degrees of freedom remains the same as in the Hubbard model and leads to no significant increase in the computational effort in spite of inclusion of the long-range Coulomb interactions. Because of the lack of large-scale computational facilities during the 1950s, such an approach was unavoidable even for relatively small molecules such as benzene. However, the remarkable fact is that in spite of so many approximations involved, PPP-model-based calculations were extremely successful in describing the electronic structure, in general, and the optical properties of π -conjugated systems, in particular (Salem 1966).

During last several years, we, along with collaborators elsewhere, have extensively used a PPP-model-based approach, to study the electronic structure and optical properties of conjugated molecules and oligomers (Ghosh et al. 2000; Shukla 2002, 2004a,b; Shukla et al. 2001, 2003, 2004; Shukla and Mazumdar 1999; Sony and Shukla 2005a,b,c, 2007, 2009). The underlying theory, along with the computational approach and the associated computer program developed in our group for dealing with the finite π -conjugated systems, has been published recently (Sony and Shukla 2010). The approach developed therein can also be applied to study graphene fragments, in addition to the aromatic hydrocarbons and conjugated polymers (Sony and Shukla 2010). We note that numerous other groups (Barford 2005; Barieswyl et al. 1992; Bursill and Barford 2009; Jug 1990; Psiachos and Mazumdar 2009; Raghu et al. 2002; Salem 1966; Soos et al. 1993; Ye et al. 2003) have also used the PPP model to study such systems. Furthermore, very recently we extended the PPP model approach also to study infinitely long one-dimensional (1D) periodic π -conjugated systems, with the aim of studying the electronic structure and the optical properties of GNRs (Gundra and Shukla 2011a,b). The Fortran 90 computer program which we developed for the purpose, along with the associated theory, has also been published recently (Gundra and Shukla 2012).

In this work, we review our PPP-model-based electronic-structure methodology applied to both finite and infinite π -electron systems, with particular emphasis on systems such as C_{60} , graphene nanodisks, and GNRs. For the finite systems, we apply the methodology both at the mean-field HF level and at the configuration-interaction (CI) level, including the influence of electron correlation effects, to study the electronic structure and optical properties of buckminster fullerene and graphene nanodisks. As far as infinite 1D systems are concerned, we study the band structure and optical properties of various GNRs and carbon nanotubes using our mean-field restricted HF (RHF) and the unrestricted HF (UHF) methodology. In particular, we probe the edge magnetism, electric-field-driven half-metallicity, linear optical absorption, and electro-absorption of various GNRs.

The remainder of this chapter is organized as follows. In Sect. 6.2 we briefly review the theory associated with the PPP model Hamiltonian and present the RHF equations for both the finite and 1D periodic systems. We present and discuss the results of various calculations on various finite and infinite systems in Sect. 6.3. Finally, in Sect. 6.4, we present our conclusions, as well as discuss possible future directions.

6.2 Theory

In this section, we briefly discuss the PPP model Hamiltonian and its HF implementations for both the finite and the periodic systems.

6.2.1 Pariser–Parr–Pople Hamiltonian

The underlying assumption in the PPP model (Pariser and Parr 1953) is that the electronic structure and optical properties of π -conjugated systems such as planar hydrocarbons can, to a very good approximation, be described strictly in terms of the dynamics of its π electrons. In other words, the σ (and the core) electrons can be assumed to be inert as far as the low-lying excitations of such systems are concerned. The reason behind the success of the σ – π separation implicit in the PPP model is that the energies of the σ electrons are so far away from the Fermi level that they are unaffected when these systems are exposed to external perturbations such as light. Of course, the influence of the core and σ electrons is incorporated implicitly in the parameters of the effective Hamiltonian. It is further assumed that (a) each carbon atom of the system contributes one π electron, represented by a p_z orbital localized on that atom (assuming that the system lies in the xy plane), and (b) the p_z orbitals form an orthonormal basis set consistent with the zero-differential overlap (ZDO) approximation developed by Parr (1952). Thus, the PPP model Hamiltonian can be expressed in the second-quantized form as

$$H_{PPP} = \sum_{i,\sigma} \epsilon_i c_{i\sigma}^\dagger c_{i\sigma} - \sum_{i,j,\sigma} t_{ij} (c_{i\sigma}^\dagger c_{j\sigma} + c_{j\sigma}^\dagger c_{i\sigma}) + U \sum_i n_{i\uparrow} n_{i\downarrow} + \sum_{i<j} V_{ij} (n_i - 1)(n_j - 1) \quad (6.1)$$

where ϵ_i represents the site energy associated with the i th carbon atom, $c_{i\sigma}^\dagger$ creates an electron of spin σ on the p_z orbital of atom i , $n_{i\sigma} = c_{i\sigma}^\dagger c_{i\sigma}$ is the number of electrons with the spin σ , and $n_i = \sum_\sigma n_{i\sigma}$ is the total number of electrons on atom i . The parameters U and V_{ij} are the on-site and long-range Coulomb interactions, respectively, while t_{ij} is the one-electron hopping matrix element. On setting $V_{ij} = 0$ (with $U \neq 0$), the Hamiltonian reduces to the Hubbard model, while on setting both $U = 0$ and $V_{ij} = 0$, the TB model is obtained. Choosing for the long-range V_{ij} , the form

$$V_{ij} = \frac{U}{\left[1 + \left(\frac{R_{ij}}{r_0}\right)^2\right]^{1/2}} \quad (6.2)$$

gives the Ohno variant (Ohno 1964) of the PPP model, whereas taking

$$V_{ij} = \frac{U}{\left[1 + \left(\frac{R_{ij}}{r_0}\right)\right]} \quad (6.3)$$

gives the Mataga–Nishimoto parametrization (Mataga and Nishimoto 1957). In the exponential version (Schulten et al. 1975), V_{ij} takes the form

$$V_{ij} = U \exp\left(-\frac{R_{ij}}{r_0}\right) \quad (6.4)$$

In Eqs. (6.2), (6.3), and (6.4), $R_{ij} = |\mathbf{r}_i - \mathbf{r}_j|$ is the distance between sites i and j in Å, while r_0 is another parameter in the same units.

In this work, we report calculations based upon the Ohno parametrization of the PPP model mentioned above (cf. Eq. 6.2). Moreover, to account for the interchain screening effects, we use a slightly modified form introduced by Chandross and Mazumdar (1997),

$$V_{ij} = U/\kappa_{ij}(1 + 0.6117R_{ij}^2)^{1/2}, \quad (6.5)$$

where κ_{ij} depicts the dielectric constant of the system which can simulate the effects of screening and R_{ij} is defined above. In various calculations performed on phenylene-based conjugated polymers including PDPAs (Ghosh et al. 2000; Shukla 2004a,b; Shukla et al. 2001, 2003, 2004; Shukla and Mazumdar 1999; Sony and Shukla 2005a), it was noticed that “screened parameters” with $U = 8.0$ eV and $\kappa_{ii} = 1.0$, and $\kappa_{ij} = 2.0$, otherwise, proposed by Chandross and Mazumdar (1997), lead to much better agreement with the experiments, as compared to the “standard parameters” with $U = 11.13$ eV and $\kappa_{i,j} = 1.0$, proposed originally by Ohno (1964). Most of the calculations in this work will be based upon these two sets of parameters, unless otherwise specified. In our computer programs implementing the PPP model at the HF level for the finite (Sony and Shukla 2010) and 1D periodic systems (Gundra and Shukla 2012), we have provided the users with the freedom to choose these “standard,” “screened” or any other user-defined parameters for the Coulomb interactions.

In order to calculate static dielectric polarizabilities for finite systems, or the electronic structure of 1D periodic systems such as the GNRs under the gated configurations, one can solve the HF equations in the presence of an external static electric field. Thus, to deal with those situations, we simply modify Eq. (6.1) under the electric dipole approximation by introducing the corresponding term containing the uniform electric field \mathbf{E} . The overall Hamiltonian of the system is then given by

$$H_{\text{PPP}}^{\text{efield}} = H_{\text{PPP}} - \boldsymbol{\mu} \cdot \mathbf{E} = H_{\text{PPP}} + |e|\mathbf{E} \cdot \mathbf{r}, \quad (6.6)$$

where H_{PPP} is the unperturbed Hamiltonian (cf. Eq. 6.1) which describes the system in the absence of the external electric field, e represents the electronic charge, $\boldsymbol{\mu} = -e\mathbf{r}$, is the dipole operator, and \mathbf{r} is the position operator.

For finite systems, we can easily go beyond the mean-field approach and perform CI on the systems concerned. For the purpose, using the Hartree-Fock molecular orbitals (MOs), one first transforms the PPP model Hamiltonian from the site representation of Eq. (6.1) to the MO representation, and subsequently CI calculations of various levels are carried out by performing virtual excitations from the occupied HF MOs to the unoccupied (virtual) MOs. If a single electron is excited from the occupied to the unoccupied orbitals, the method is called singles-CI (SCI) method; if two electrons are excited in this way, it is called the singles-doubles-CI

(SDCI) method; and so forth. When up to two electrons are virtually excited with respect to multiple reference configurations, the approach is called the multi-reference SDCI (MRSDCI) method. The MRSDCI approach is quite powerful when it comes to dealing with systems with strong electron correlations, as well as in obtaining accurate representation of the excited states. In our PPP-model-based calculations of the electronic structure and optical properties of conjugated polymers, we have made extensive use of the MRSDCI approach (Ghosh et al. 2000; Shukla 2002, 2004a; Shukla et al. 2001, 2003, 2004; Shukla and Mazumdar 1999; Sony and Shukla 2005a,b,c, 2007, 2009).

Going beyond the HF approach for periodic infinite systems is more complicated, and in future, we plan to implement the approaches aimed at achieving that goal.

6.2.2 Hartree-Fock Equations

For the sake of completeness, we present the RHF equations corresponding to the PPP model, first for the finite systems and then for infinite periodic systems. Details for the corresponding UHF equations can be found in our earlier publications (Gundra and Shukla 2012; Sony and Shukla 2010).

6.2.2.1 Finite Systems

The RHF approach is applicable when the system is a closed-shell one, with an even number of π electrons, so that each molecular orbital (MO) is doubly occupied with an up- and a down-spin electron. We solve the RHF equations using the linear combination of atomic orbitals (LCAO) approach, in which each MO is expressed as a linear combination of a finite-basis set

$$\psi_{\mu} = \sum_i C_{i\mu} \phi_i, \quad (6.7)$$

where ψ_{μ} represents the μ th MO of the system, ϕ_i 's represent the p_z -orbitals localized on various carbon atoms, and the determination of the unknown linear coefficients $C_{i\mu}$ amounts to the solution of the RHF equations. As per the ZDO approximation (Parr 1952), atomic orbitals, ϕ_i 's, are assumed to form an orthonormal basis set. Using the conjecture of Eq. (6.7) in conjunction with the Hamiltonian above, one obtains the RHF equations in the matrix form

$$\sum_j (F_{ij} - \varepsilon_{\mu}) C_{j\mu} = 0, \quad (6.8)$$

where ε_{μ} is the RHF eigenvalue of the μ th MO; F_{ij} is the Fock matrix defined by the equations

$$F_{ij} = t_{ij} - \frac{1}{2} P_{ij} V_{ij}, \quad (i \neq j) \quad (6.9)$$

$$F_{ii} = \epsilon_i - \sum_{j \neq i} V_{ij} + \sum_j P_{jj} V_{ij} - \frac{1}{2} P_{ii} V_{ii}, \quad (i = j) \quad (6.10)$$

where ϵ_i , t_{ij} and V_{ij} are defined above (cf. Eq. 6.1); and P_{ij} is the density matrix element, defined as

$$P_{ij} = 2 \sum_{\mu=1}^{n_{\text{occ}}} C_{i\mu}^* C_{j\mu}, \quad (6.11)$$

where $n_{\text{occ}} = N_{\text{el}}/2$ denotes the number of occupied orbitals for a system in which the number of π electrons is N_{el} . Once the Fock matrix is constructed, one diagonalizes it to obtain a new set of orbitals and density matrix, and the process is repeated until self-consistency is achieved.

6.2.2.2 Periodic Systems

The RHF method is applicable to periodic systems with an even number of electrons per unit cell, so that each band is doubly occupied. In principle, the RHF theory for periodic systems is identical to that for finite systems, except for the additional complications due to the Bloch nature of the orbitals. Next, we briefly review the RHF theory for 1D periodic systems when the PPP model is utilized. The μ th doubly occupied Bloch orbital of the system, corresponding to the crystal momentum k , is expressed as a linear combination of m basis functions per unit cell,

$$\psi_{\mu}(k) = \sum_{i=1}^m C_{i\mu}(k) \phi_i(k), \quad (6.12)$$

where $C_{i\mu}(k)$'s represent the linear expansion coefficients, to be determined at a set of k -points in the 1D BZ, and the i th Bloch function $\phi_i(k)$ is given by

$$\phi_i(k) = \frac{1}{\sqrt{N}} \sum_l e^{ikR_l} \phi_i(r - R_l), \quad (6.13)$$

where $N \rightarrow \infty$ is the total number of unit cells in the system and $\phi_i(r - R_l)$ is the i th atomic orbital (AO) (p_z orbital mentioned in Sect. 6.2.1) located in the l th unit cell defined by the lattice vector R_l . It is easy to verify that the Bloch basis functions $\phi_i(k)$ will form an orthonormal set owing to the orthonormality of the p_z basis functions $\phi_i(r - R_l)$, leading to the simplified RHF equations in the matrix form

$$F(k)C_{\mu}(k) = \epsilon_{\mu}(k)C_{\mu}(k), \quad (6.14)$$

where, for a given k value, $F(k)$ represents the Fock matrix, $C_\mu(k)$ represents the corresponding $C_{i\mu}(k)$ coefficients, arranged in the form of a column vector, and $\varepsilon_\mu(k)$ denotes the band eigenvalue. The Fock operator is given by

$$F(k) = h(k) + (J(k) - \frac{1}{2}K(k)) \quad (6.15)$$

above $h(k)$, $J(k)$, and $K(k)$ are obtained by Fourier transforming the one-electron, direct, and exchange integrals corresponding to the PPP Hamiltonian (cf. Eq. 6.1), using the general formula

$$O_{ij}(k) = \sum_{l=-\infty}^{\infty} e^{ikR_l} O_{ij}(R_l), \quad (6.16)$$

where $O_{ij}(R_l)$ denotes the matrix elements of a general real-space one-electron operator O . In particular, the real-space versions of the Coulomb and the exchange integrals $J_{ij}(R_l)$ and $K_{ij}(R_l)$ for the PPP model are given by

$$J_{ij}(R_l) = \sum_{p=1}^m V_{i(o)k(R_l)} D_{pp}(o) \delta_{ij}, \quad (6.17)$$

and

$$K_{ij}(R_l) = V_{i(o)j(R_l)} D_{ij}(R_l), \quad (6.18)$$

where $V_{i(o)j(R_l)}$ denotes the long-range part of the Coulomb interaction of the PPP Hamiltonian assuming that the basis function i is located in the reference unit cell, while j is located in the unit cell labeled by R_l . Therefore, $V_{i(o)j(R_l)}$ can be computed using any of the Coulomb parametrization described in Sect. 6.2.1, and the density matrix elements $D_{ij}(R_l)$ are given by

$$D_{ij}(R_l) = \frac{2}{\Delta} \int \sum_{\mu=1}^{n_{\text{occ}}} C_{i\mu}^*(k) C_{j\mu}(k) e^{ikR_l} dk, \quad (6.19)$$

where the integral over k is performed over the 1D BZ of length Δ and n_{occ} denotes the number of occupied Bloch orbitals per unit cell. The total energy per unit cell of a given system is computed using the real-space expression

$$E_{\text{cell}} = \sum_l \sum_{i,j} D_{ij}(R_l) \left\{ h_{ij}(R_l) + J_{ij}(R_l) - \frac{1}{2} K_{ij}(R_l) \right\}. \quad (6.20)$$

The RHF equations of the system, leading to the band structure ($\varepsilon_\mu(k)$) and the corresponding Bloch orbitals, can be solved by iterative diagonalization technique applied to Eq. (6.14) at a set of k -points, until the total energy per cell of the system (cf. Eq. 6.20) converges. We have recently numerically implemented the approach

outlined here to solve both the RHF and the UHF equations for 1D periodic systems, within the PPP model (Gundra and Shukla 2012). In our program (Gundra and Shukla 2012), during the self-consistent HF iterations, the integration over the BZ is performed using the Gauss-Legendre quadrature technique as suggested by André et al. (1984), with the additional flexibility that the number of points used for the quadrature can be chosen by the user.

6.3 Applications

In this section, we demonstrate our approach by applying it first to the finite systems and next to 1D periodic infinite systems.

6.3.1 Finite Systems

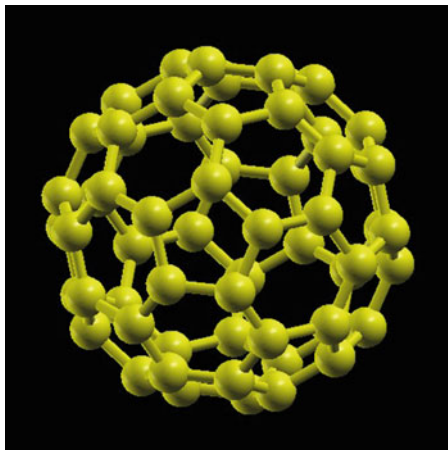
As far as finite systems are concerned, in our previous papers, we have applied our PPP-model-based approach to study the electronic structure and the optical properties of the oligomers of a number of conjugated polymers such as poly(di)phenyl-polyacetylene (PDPA) (Ghosh et al. 2000; Shukla 2004b; Shukla et al. 2001; Shukla and Mazumdar 1999; Sony and Shukla 2005a,b), poly-phenylene-vinylene (PPV) (Shukla 2002; Shukla et al. 2003, 2004), and polyacenes (Sony and Shukla 2005c, 2007, 2009). In what follows, we demonstrate our approach by applying it to study the optical properties of two systems: (a) fullerene C_{60} and (b) graphene nanodisks.

6.3.1.1 Optical Properties of Fullerene C_{60}

Because of its curved geometry, strictly speaking, fullerene C_{60} is not a π -electron system. Nevertheless, we can treat it as an approximate π -electron system given that each carbon atom possesses an electron which can be called a π electron in a local sense, described by a p orbital directed perpendicular to the fullerene surface at that atom. Because of that reason, several authors have used the PPP model, and the related Hubbard and the extended Hubbard models, to study the electronic structure, dielectric response, and optical properties of C_{60} , both at the SCF and the CI levels (Harigaya and Abe 1994; Kim and Su 1994; László and Udvardi 1987, 1989; Ruiz et al. 2001, 1998). Next, we perform SCI calculations, within the PPP model, to calculate the linear optical absorption spectrum of C_{60} . We also calculate the energy of the lowest triplet excited state using the same approach and compare our results to the experiments wherever possible.

As illustrated in Fig. 6.1, we consider the soccer ball configuration of C_{60} , corresponding to the point group I_h , with hexagons and pentagons on its surface.

Fig. 6.1 Soccer ball structure of C_{60} considered in these calculations



The nearest-neighbor C–C distances in C_{60} can be classified as “single bonds” and “double bonds,” with the single bonds being the sides shared between a pentagon and a hexagon, while the double bonds are those shared between two hexagons. In these calculations we took the double bond length to be 1.39 Å, and the single bond length as 1.45 Å, as obtained by Greer using an ab initio density-functional theory-based approach (Greer 2000). In these calculations, we included only the nearest-neighbor hoppings, computed using the relation $t_{ij} = t_0 \exp[-\beta(\frac{r_{ij}}{a} - 1)]$ (Kim and Su 1994), with $t_0 = -2.4$ eV, $\beta = 3.6$, $a = 1.40$ Å, and r_{ij} being the distance between sites i and j . This yields the values of the hopping matrix elements $t_D = -2.462$ eV and $t_S = -2.111$ eV, for the double bond and the single bond, respectively. Using these hopping matrix elements and bond lengths, coupled with the Ohno parametrization of the Coulomb matrix elements using both the standard and the screened parameters, we first performed the RHF calculations on C_{60} to obtain its MOs, which were subsequently used to perform the correlated SCI calculations on the system, which provides us with a representation of not just the ground state but also its various excited states. These SCI level excited states for the spin-singlet states were used to compute the linear optical absorption spectrum of C_{60} , employing the electric-dipole approximation, and the Lorentzian line shapes.

Before discussing the optical absorption spectrum of C_{60} , we briefly discuss its electronic structure. The highest occupied molecular orbital (HOMO) of C_{60} is five-fold degenerate and belongs to the irreducible representation (irrep) h_u of the point group I_h . The lowest unoccupied molecular orbital (LUMO), on the other hand, is threefold degenerate and belongs to the irrep t_{1u} . Because the HOMO and LUMO have the same symmetry under the inversion operator, electric dipole transitions are forbidden between them, and no absorption takes place at the HOMO-LUMO gap. We present our PPP-model-based SCI optical absorption spectrum in Fig. 6.2, computed using both the standard and the screened Coulomb parameters discussed earlier in Sect. 6.2.1. From the plots, it is obvious that quantitatively speaking the

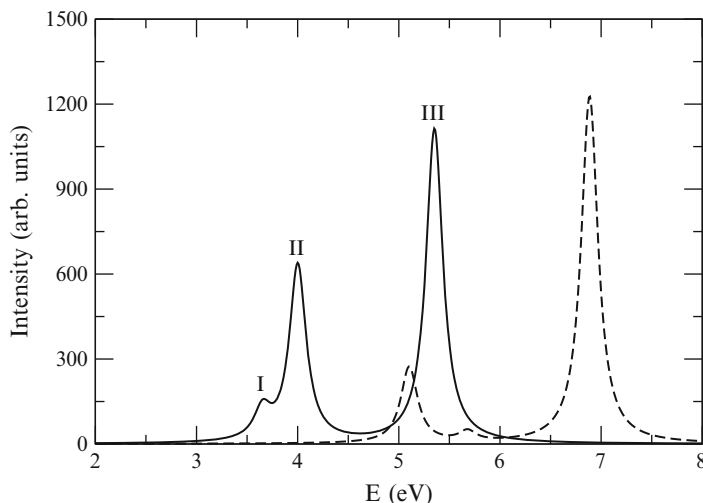


Fig. 6.2 Optical absorption spectra of C_{60} , computed using the SCI approach, within the PPP model employing the screened parameters (*solid line*) and the standard parameters (*dashed line*). A Lorentzian line shape, along with a line width of 0.1 eV, was used to plot the spectra

standard-parameter-based spectrum is substantially blue-shifted compared to the screened parameter spectrum. Furthermore, there are some qualitative difference also between the two calculations in that the relative intensities of the first two peaks are just reverse of each other. When compared to the optical absorption experiments on C_{60} (Ajje et al. 1990; Gasyna et al. 1991; Leach et al. 1992; Lee et al. 1992; Ren et al. 1991), our screened parameter-based results are in much better agreement with it, as compared to the standard parameter ones. Therefore, henceforth, we restrict our discussion only to our screened parameter spectrum which exhibits three prominent absorption peaks labeled I, II, and III in Fig. 6.2. In its ground state, C_{60} is a closed-shell system in the 1A_g state; therefore, as per selection rules, it can make an electric-dipole transition only to excited states belonging to ${}^1T_{1u}$ irrep. Indeed, all the three labeled peaks in the plotted spectrum correspond to threefold degenerate excited states, consistent with the dimension of the T_1 irrep. In Fig. 6.2, peaks I, II, and III are located at 3.67, 4.00, and 5.35 eV, respectively. Relative intensities and general features of our screened parameter-based spectrum agree quite well with the measured spectrum of C_{60} reported by Gasyna et al. (1991), who also reported three major absorption bands of increasing intensities located at 3.81, 4.91, and 5.97 eV. Given that our calculations have been performed using the SCI method, which does not include the electron-correlation effects in a sophisticated manner, the agreement between the theory and experiments is quite reasonable. At present a large-scale MRSDCI calculation of the electric-dipole optical transitions in C_{60} , employing the PPP model, is under way in our group, and the results will be published in future.

Next, we discuss the lowest triplet excited state of C_{60} , the 1^3T_{2g} state. The wave function of this state is dominated by the configuration with singly occupied HOMO and LUMO orbitals, along with triplet spin multiplicity. Our PPP-model-based SCI

value of 2.42 eV for the excitation energy of this state is in excellent agreement the value 2.46 eV reported by [László and Udvardi \(1987\)](#), also based upon the PPP-SCI approach, although using a different set of Coulomb parameters. Experimentally speaking, the exact value of the excitation energy of this state appears not to be very certain, although [Leach et al. \(1992\)](#) have reported the onset of triplet absorption near 1.78 eV.

6.3.1.2 Optical Absorption Spectrum of Graphene Nanodisks

Because of the gapless nature of 2D graphene, its device applications are extremely limited. That is one of the reasons behind the considerable amount of research effort in the field of reduced dimensional nanostructures of graphene such as quasi-1D GNRs ([Barone et al. 2006](#); [Palacios et al. 2010](#); [Prezzi et al. 2008](#); [Son et al. 2006a](#); [Yang et al. 2007a,b, 2008](#)) and 0D graphene nanodisks ([Ezawa 2008](#); [Fernández-Rossier and Palacios 2007](#); [Güçlü et al. 2009](#); [Hod et al. 2008](#); [Kinza et al. 2010](#); [Ridder and Lyding 2009](#); [Schumacher 2011](#); [Wang et al. 2008, 2009](#); [Yazyev 2010](#)), which are also called graphene quantum dots or graphene nanoflakes. Graphene nanodisks, which are nothing but finite-sized graphene fragments, can, in general, be of any shape, regular or irregular. Regular-shaped nanodisks are characterized by their shapes as well as by the nature of their edges, which can be of the zigzag type or the armchair type. Some of the regular-shaped graphene nanodisks which have been studied in the literature are shown in Fig. 6.3. For example, triangular graphene nanodisks with zigzag edges shown in Fig. 6.3a have been theoretically predicted to have magnetic ground states ([Fernández-Rossier and Palacios 2007](#); [Güçlü et al. 2009](#); [Kinza et al. 2010](#); [Wang et al. 2008, 2009](#); [Yazyev 2010](#)). Optical properties of graphene nanodisks were recently studied theoretically by Schumacher ([Schumacher 2011](#)) using a time-dependent density functional theory-based approach. Because of their interesting optical and magnetic properties, graphene nanodisks have potential applications in the field of optoelectronics and spintronics ([Yazyev 2010](#)).

In this work, we present the calculations of the linear optical absorption spectrum of the nanodisks shown in Fig. 6.3, using our PPP-model-based approach, employing the screened Coulomb parameters and the SCI method. The aim of this work is to understand the optical properties of graphene nanodisks and, particularly, to probe the influence of the shape of the nanodisks on their absorption spectra. We note that except for the zigzag triangular nanodisk (cf. Fig. 6.3a), which has an odd number of π electrons, and hence an open shell doublet ground state, the rest of the nanodisks have an even number of π electrons, and a closed-shell singlet ground state. Results of our calculations for various nanodisks are presented in Fig. 6.4. On comparing the absorption spectra of various nanodisks, the following trends emerge: (a) for the triangular zigzag nanodisk, the absorption starts with a very weak feature near 4 eV, while the most intense absorption occurs at energies higher than 7 eV; (b) for the triangular armchair nanodisk, the most intense absorption occurs for

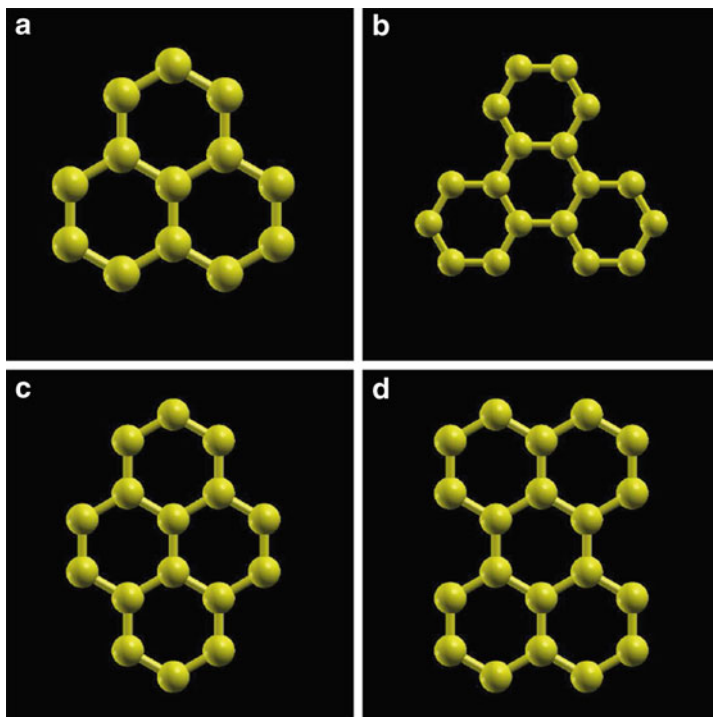


Fig. 6.3 Structures of a few symmetric graphene nanodisks. (a) Zigzag triangular. (b) Armchair triangular. (c) Diamond shaped. (d) Bowtie shaped

the first peak of the spectrum located at 4.4 eV, with somewhat weaker features at higher energies; (c) for the diamond-shaped disk, the first peak which is reasonably strong occurs at even lower energy close 3.2 eV, with several intense peaks at higher energies; and (d) in the bowtie-shaped disk, the optical absorption starts at the lowest energy (≈ 2.6 eV) of all the nanodisks described considered here, with stronger peaks at higher energies as well. Thus, we see an obvious correlation between the shapes of the nanodisks, and their absorption spectra. Furthermore, for the triangular nanodisks, the nature of edges (armchair vs. zigzag) also influences the optical absorption both qualitatively and quantitatively. Therefore, it is conceivable that one can determine the shapes and edge structures of graphene nanodisks through optical absorption spectroscopy.

As far as the nature of excited states contributing to the optical absorption in various nanodisks is concerned, a common feature emerges. In all the nanodisks, the first absorption peak is characterized by an excited state which mainly consists of the configuration obtained by a single-electron excitation from the HOMO to the LUMO orbital. A more detailed study of the optical absorption in graphene nanodisks, including higher-level CI treatments and the influence of disorder, will be published elsewhere in future.

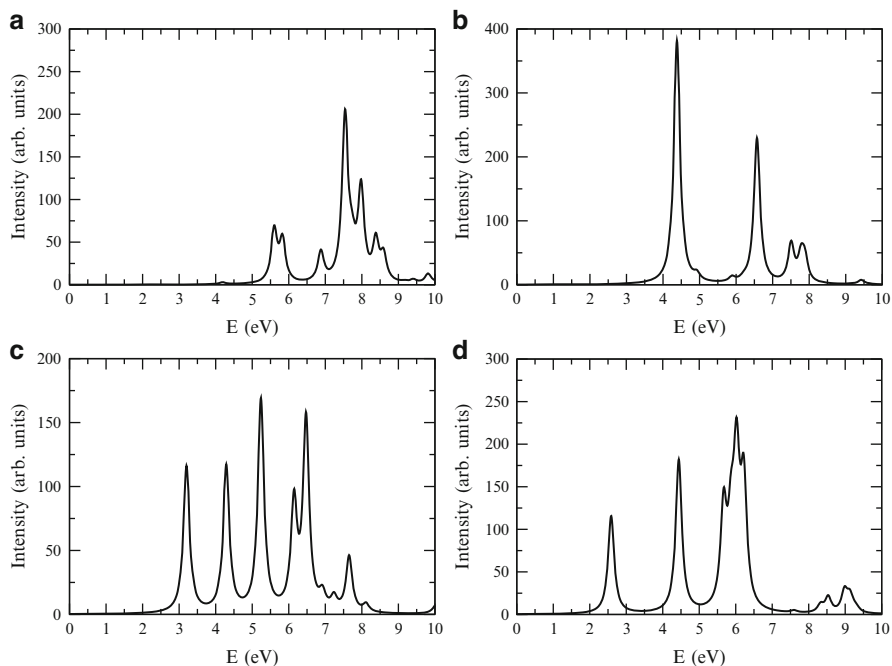


Fig. 6.4 Linear optical absorption spectra of various graphene nanodisks computed using the PPP-SCI approach and screened Coulomb parameters. A uniform line width of 0.1 eV was used to plot all the spectra. (a) Zigzag triangular. (b) Armchair triangular. (c) Diamond shaped. (d) Bowtie shaped

6.3.2 Infinite 1D Periodic Systems

As far as infinite 1D periodic systems are concerned, we apply our approach to study the band structure and optical properties of mono- and multilayer-GNRs, and single-walled carbon nanotubes.

6.3.2.1 Band Structure of Graphene Nanoribbons

GNRs are quasi 1D structures which can be obtained by patterning graphene using various techniques (Han et al. 2007). Unlike monolayer graphene, GNRs exhibit energy band gaps (Son et al. 2006a) much needed for device applications. Theoretical works on GNRs mainly focus on ribbons with armchair edge termination known as armchair GNRs (AGNRs) and zigzag edge termination known as zigzag GNRs (ZGNRs). The structures of an AGNR, and a ZGNR, are shown in Figs. 6.5a and b

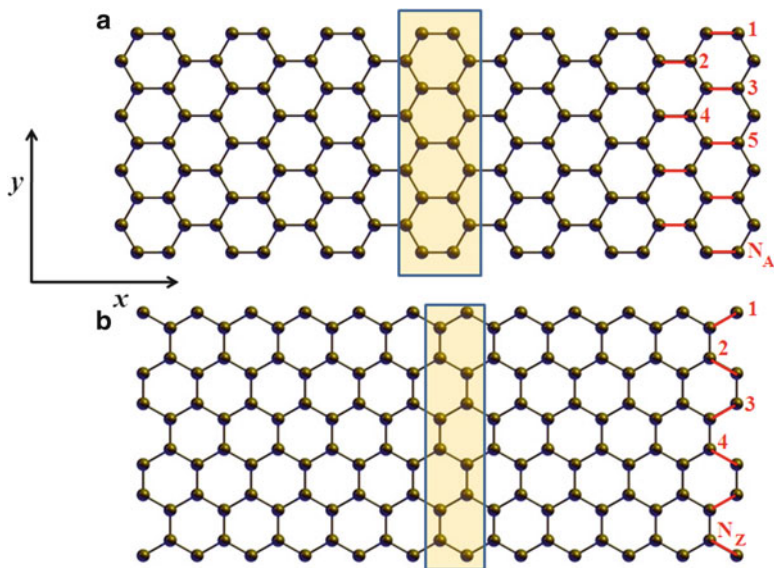
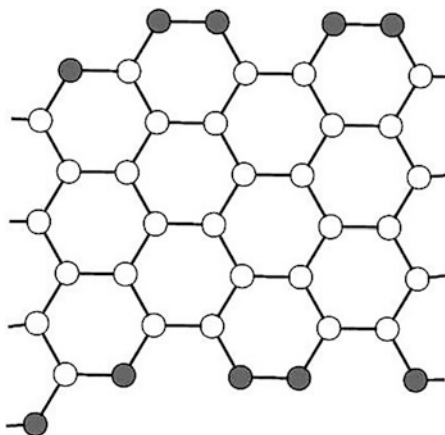


Fig. 6.5 The schematic representation of (a) armchair graphene nanoribbon with $N_A = 9$ and (b) zigzag graphene nanoribbon with $N_Z = 6$. The ribbons are assumed to lie in the xy plane, with the periodicity in the x -direction. The unit cells of these ribbon are enclosed in the shaded rectangles

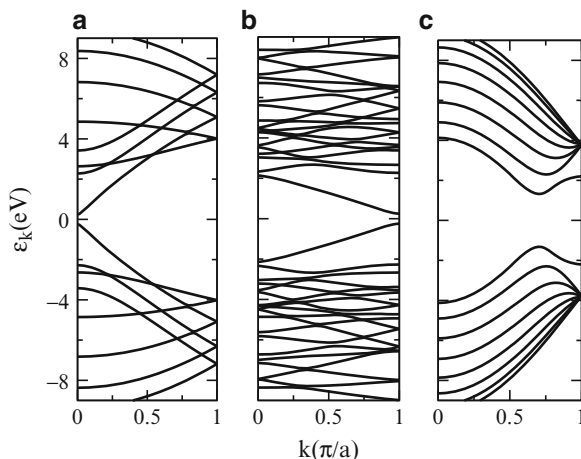
Fig. 6.6 The unit cell of a general GNR with eight dimer lines across the width



respectively. In the case of AGNRs, N_A denotes the number of carbon-carbon dimer lines across the width (cf. Fig. 6.5a), while in the case of ZGNRs, width N_Z denotes the number of zigzag lines (cf. Fig. 6.5b) across the width.

In addition to the GNRs with well-defined edge terminations such as the AGNRs and the ZGNRs, we also present calculations on general GNRs, which possess mixed type of edge terminations, including both the armchair and zigzag edges. The schematic structure of such a general GNR is presented in Fig. 6.6, in which

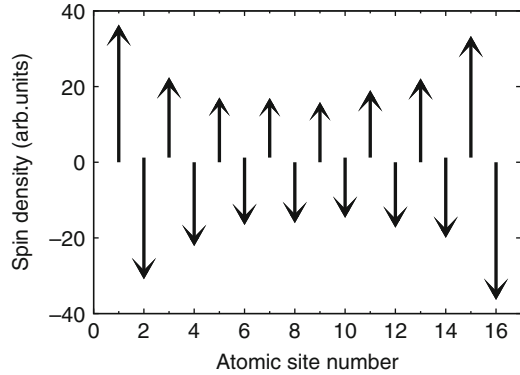
Fig. 6.7 Band structure of (a) AGNR-8 obtained using PPP-RHF method, (b) general GNR (cf. Fig. 6.6) obtained using PPP-RHF method, and (c) ZGNR-8 obtained using PPP-UHF method



the atoms at the edges are represented by solid circles. An armchair edge can be identified by a dimer line connecting two edge atoms, whereas a zigzag edge can be identified by an edge atom which is connected only with the atoms in the bulk of the ribbon.

In all the calculations performed on GNRs of any type, the carbon-carbon nearest-neighbor distance was taken to be 1.42 \AA , and all the bond angles were assumed to be 120° . In case of multilayer GNRs, the distance between the adjacent layers was taken to be 3.35 \AA . The hopping is restricted only to the nearest neighbors within each layer, and between the adjacent layers, with the values $t = 2.7 \text{ eV}$ (intraplane), and $t_\perp = 0.4 \text{ eV}$ (inter-plane) respectively. As far as the Coulomb parameters are concerned, we have used the screened parameters of Chandross and Mazumdar (Chandross and Mazumdar 1997), with $U = 8.0 \text{ eV}$ and $\kappa_{i,j} = 2.0$ ($i \neq j$) and $\kappa_{i,i} = 1$. The band structures of AGNR-8 (AGNR- N_A denotes an AGNR with width N_A), and the general GNR, obtained using the PPP-RHF method are presented in Figs. 6.7a and b, respectively. It is evident from Fig. 6.7 that all the GNRs exhibit finite band gaps, and their band structures depend crucially on their geometry. A band gap of 0.5 eV was observed at $k = 0$ for AGNR-8 (cf. Fig. 6.7a). It is worth mentioning that AGNR-8 is metallic at the TB level. In fact depending on the value of N_A , AGNRs are classified into three categories with $N_A = 3p$, $3p + 1$, and $3p + 2$, p being an integer. At the TB level, all the AGNRs with $N_A = 3p + 2$ are predicted to be gapless (Nakada et al. 1996). However, ab initio DFT calculations predict all types of AGNRs to be gapped (Son et al. 2006a). As far as the PPP-model-based calculations are concerned, the long-range electron–electron interactions which it incorporates play a crucial role in opening the band gaps in $3p + 2$ class AGNRs (Gundra and Shukla 2011a). In case of the general GNR, the band gap is direct in nature, with the value 0.49 eV , located at $k = \pi$. Furthermore, as is obvious from Fig. 6.7, band structure of the general GNR is significantly different from those of both the AGNR and the ZGNR.

Fig. 6.8 The spin density distribution of ZGNR-8 obtained using PPP-UHF method, plotted at various atomic sites in the unit cell across the width



In the case of ZGNRs, the ground state is predicted to be magnetic with oppositely oriented spins localized on the zigzag edges located on the opposite sides of the ribbons (Son et al. 2006a). The ZGNRs are gapless at the TB level, characterized by flat bands near the Fermi energy (E_F), leading to a van Hove singularity at E_F , suggesting an instability. And indeed, a symmetry broken state with magnetic ordering mediated by Coulomb interactions (Son et al. 2006b) stabilizes the system. We obtain this broken-symmetry ground state exhibiting edge magnetism on performing the PPP-UHF calculations (Gundra and Shukla 2011a), which are based upon separate mean-fields for the up- and the down-spin electrons. On the other hand, the PPP-RHF method, by its very nature, predicts a nonmagnetic ground state for ZGNRs which has a higher energy per unit cell as compared to that obtained for the spin-polarized state using the PPP-UHF method. The band structure of ZGNR-8 (ZGNR- N_Z denotes a ZGNR with width N_Z) obtained using PPP-UHF approach is presented in Fig. 6.7c. A significant band gap of 2.64 eV is opened up at $k = \frac{2\pi}{3}$ because of the magnetic ordering. The spin density distribution for ZGNR-8, plotted for the sites across its width, presented in Fig. 6.8 clearly exhibits edge magnetism. The electrons of different spins are localized at adjacent sites along the width, indicating an antiferromagnetic order. However, a ferromagnetic order is observed on a given edge, along its length (Gundra and Shukla 2012).

6.3.2.2 Band Structure of Gated Graphene Nanoribbons

GNRs display interesting electronic properties in the presence of an external gate bias. For example, ZGNRs exhibit half-metallic behavior in the presence of a lateral electric field (E_y), i.e., ZGNRs are conducting for the electrons of one spin and insulating for those of the other spin (Son et al. 2006b). Therefore, gated ZGNRs have potential device applications in the field of spintronics.

This is illustrated in Fig. 6.9 in which the band structure of ZGNR-12 in the presence of a lateral electric field of strength 0.2 V/Å is presented. While the bands of the up (α) and down (β) spin electrons are degenerate in the absence of the

Fig. 6.9 Band structure of ZGNR-12 in the presence of lateral electric field of strength 0.2 V/\AA . The *solid lines* represent the bands corresponding to electrons of spin- α , and the *broken lines* represent the bands corresponding to electrons of spin- β

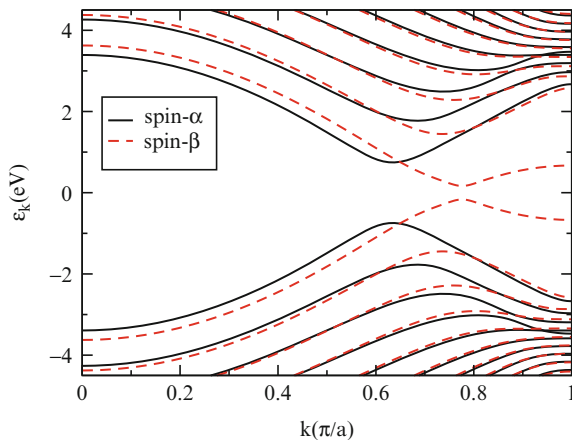
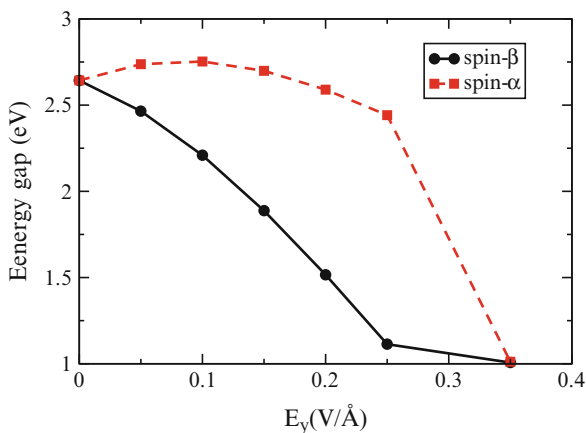


Fig. 6.10 Variation of energy band gaps with electric field applied along y -axis of ZGNR-8, obtained using the PPP-UHF method. The *solid black line* represents energy gaps for spin-down electrons, and the *red broken line* represents energy gaps for spin-up electrons



field with a band gap of 2.1 eV, the degeneracy is lifted in the presence of external electric field (E_y) along y -axis, and the band gap for electrons of spin- α changes to 1.5 eV, while that for electrons of spin- β reduces drastically to 0.3 eV, indicating the tendency towards the half-metallic nature. The half-metallic nature of ZGNRs can be understood from the fact that in the absence of external electric field, oppositely oriented spin states are localized on the opposite edges of the ribbon. In the presence of a nonzero E_y , the ZGNR develops a potential difference across its width, thereby energies of the localized edge states are increased on one edge and decreased on the other one, leading to different band gaps for the electrons of different spin orientations (Son et al. 2006b). With the increasing field strength E_y , the band gaps of spin- β electrons tend to decrease, while those of α electrons exhibit a slight increase up to a certain field strength, beyond which they also decrease monotonically. After a critical field strength, the energy gaps for electrons of both spins attain the same value, and the half-metallic behavior exhibited by the ZGNRs disappears. To illustrate this point, in Fig. 6.10 we present the variation of band gaps

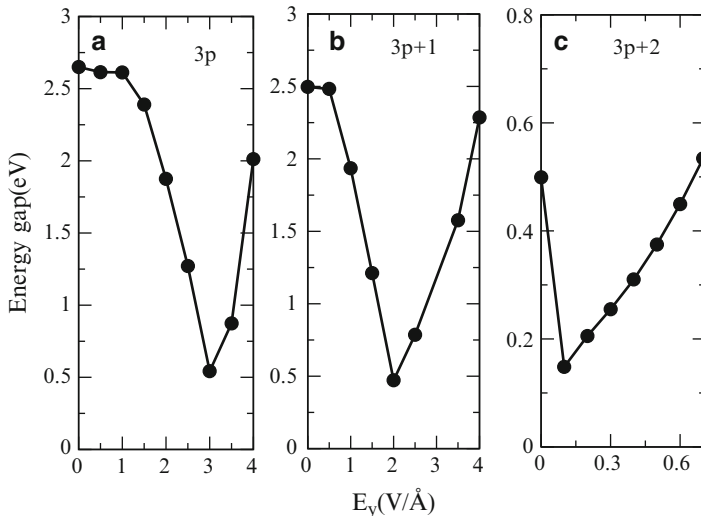


Fig. 6.11 Variation of the band gaps of the AGNRs with respect to the electric field applied along the y -axis, for (a) $N_A = 3p$, (b) $N_A = 3p + 1$, and (c) $N_A = 3p + 2$, with $p = 2$

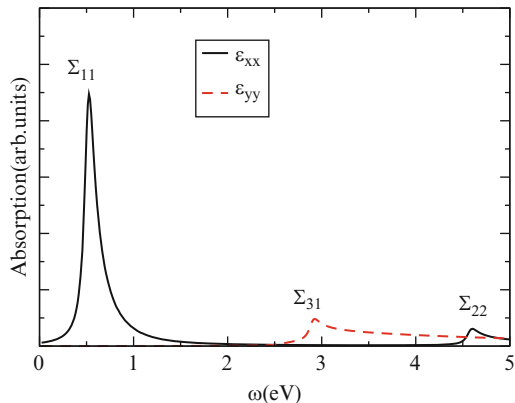
of spin- α and spin- β electrons with E_y for ZGNR-8, calculated using the PPP-UHF method. The half-metallic nature is observed when $0 \leq E_y \leq 0.35$ V/Å, with band gaps for electron of spin- α and spin- β being well separated, and for $E_y > 0.35$ V/Å, the energy gaps for electrons of both the spins are again identical, with the value of the band gap being lower than the corresponding value in the absence of E_y . Thus, the half-metallic behavior disappears for $E_y > 0.35$ V/Å. The first-principles DFT-based calculations by Kan et al. (2007) also predicted a similar behavior in ZGNRs.

The external electric field has profound effect on the band gaps of AGNRs as well. We illustrate the variation of band gaps with E_y for AGNRs of width $N_A = 3p$, $3p + 1$ and $3p + 2$, for $p = 2$ in Fig. 6.11. In all the ribbons the gap decreases initially with increase in the strength of E_y . But beyond a critical field strength (E_y^c), a reverse trend is observed, where the gap increases with further increase in the field strength. Even though we have presented the results corresponding to $p = 2$, a similar behavior is observed for $p > 2$ as well. We observe that in each category of AGNRs, the value of E_y^c decreases with the increase in their width, e.g., we have obtained $E_y^c = 3$ V/Å for AGNR-6, whereas the corresponding value for AGNR-9 is 2 V/Å.

6.3.2.3 Optical Properties of Graphene Nanoribbons

As discussed earlier, the geometry of GNRs plays a crucial role in determining their electronic structure. Therefore, the optical properties of the ribbons will also be quite sensitive to their geometry, thereby allowing the possibility of determining

Fig. 6.12 Optical absorption spectrum of AGNR-8 calculated by the PPP-RHF method. The *solid black line* represents $\epsilon_{xx}(\omega)$, while the *dotted red line* represents $\epsilon_{yy}(\omega)$. A line width of 0.05 eV was assumed

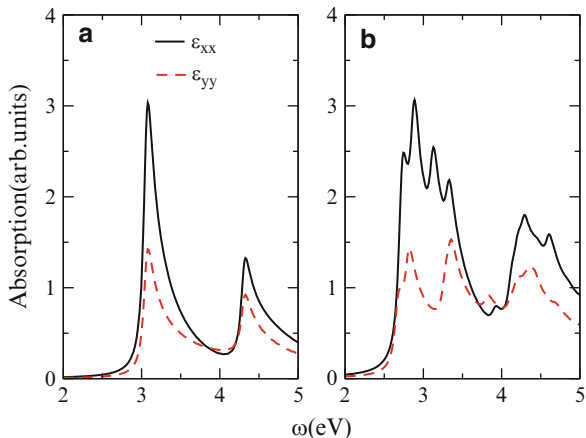


the geometry of GNRs by means of optical measurements. Next, we present results of our calculations of the optical absorption spectra of various GNRs and CNTs, for the incident radiation polarized in x (or longitudinal) or y (or transverse) directions, computed in the form of $\epsilon_{xx}(\omega)$ and $\epsilon_{yy}(\omega)$, respectively, where $\epsilon_{ii}(\omega)$ denotes the imaginary part of the dielectric constant tensor for the i th Cartesian component and ω denotes the frequency of incident photons. The calculations of various components of the $\epsilon_{ii}(\omega)$ were performed using the standard approach outlined in our previous publications (Gundra and Shukla 2011a,b, 2012). The optical absorption spectrum of AGNR-8, obtained using the PPP-RHF method, is displayed in Fig. 6.12. If Σ_{mn} denotes a peak in the spectrum due to a transition from m th valence band (counted from top) to the n th conduction band (counted from bottom), the peak of $\epsilon_{xx}(\omega)$ at 0.54 eV is Σ_{11} , and the peak at 4.60 eV is Σ_{22} . Whereas, the peak in $\epsilon_{yy}(\omega)$ at 2.93 eV corresponds to Σ_{31} . The individual peaks in the absorption spectrum of AGNR-8 are well separated in energy and correspond to either x - or y -polarized photons, consistent with the dipole selection rules of D_{2h} point group symmetry of AGNRs.

In Fig. 6.13a we present the optical absorption spectrum of ZGNR-6 computed using the PPP-UHF method. Even though the point group of ZGNRs is also D_{2h} , in contrast to AGNRs, most of the prominent peaks of ZGNR-6 exhibit mixed polarization characteristics. This is due to the fact that the edge-polarized magnetic ground state of ZGNRs no longer exhibits D_{2h} symmetry, because the reflection symmetry about the xz -plane is broken, thereby leading to mixed polarizations in the optical absorption. Thus, by using optical probes, one can predict whether a given ribbon is an AGNR or a ZGNR by analyzing the polarization characteristics of the absorption peaks.

Apart from determining the geometry of GNRs, optical absorption spectra can also be used to differentiate the monolayer GNRs from the bilayer and the multilayer GNRs. We illustrate this by comparing the optical absorption spectrum of monolayer ZGNR-6 with that of its bilayer counterpart. Similar to the case of monolayer ZGNR-6, most of the prominent peaks of bilayer ZGNR-6 also exhibit

Fig. 6.13 Optical absorption spectrum of (a) ZGNR-6 and (b) bilayer-ZGNR-6, obtained by the PPP-UHF method. The solid black line represents $\epsilon_{xx}(\omega)$, while the dotted red line represents $\epsilon_{yy}(\omega)$. A line width of 0.05 eV was assumed



mixed polarization characteristics (cf. Fig. 6.13b) due to edge magnetism (Castro et al. 2007). However, it is interesting to note that in the case of monolayer ZGNRs, the shape of the spectra corresponding to $\epsilon_{xx}(\omega)$ and $\epsilon_{yy}(\omega)$ remains similar, though the magnitude of peaks of $\epsilon_{yy}(\omega)$ is smaller when compared to those of $\epsilon_{xx}(\omega)$. This scenario is completely changed in the case of bilayer ZGNR-8, in which due to the presence of second layer, many additional peaks are observed in $\epsilon_{xx}(\omega)$ as compared to $\epsilon_{yy}(\omega)$. Therefore, the optical response of monolayer ZGNRs is quite different from that of the bilayer ZGNRs and can, in principle, be used to distinguish between them through optical measurements.

6.3.2.4 Band Structure and Optical Properties of Bilayer AGNRs

Bilayer and multilayer AGNRs exhibit interesting electronic and optical properties which we have investigated in an earlier publication (Gundra and Shukla 2011b). For example, the intensity of the linear optical absorption in multilayer AGNRs increases rapidly with the increasing number of layers and depends crucially on the relative orientation of adjacent layers (Gundra and Shukla 2011b). In this section, we discuss the band structure and optical properties of bilayer AGNR-8 obtained using the PPP-RHF method. We assume Bernal stacking for bilayer AGNRs and consider two types of edge alignments, namely, α alignment and β alignment, shown schematically in Fig. 6.14 (Gundra and Shukla 2011b). To illustrate the influence of edge alignment on the electronic structure of bilayer AGNRs, we present the band structure of bilayer AGNR-8 in α and β alignments in Figs. 6.15a and b, respectively. The individual energy bands near Fermi energy are separated by larger energy in α alignment when compared to β alignment (Gundra and Shukla 2011b). This has important implications on the optical absorption spectra which is presented in Figs. 6.15c and d, for the two alignments. It is obvious that the optical absorption spectra for the two alignments are substantially different from each

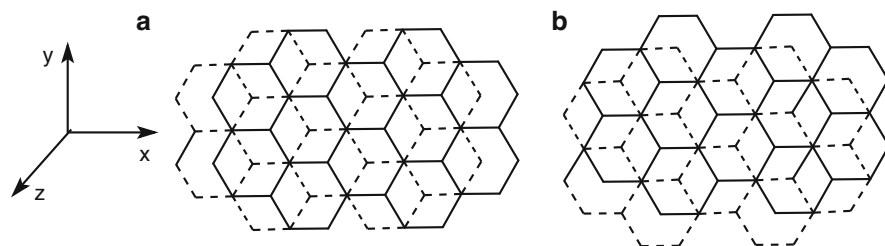


Fig. 6.14 Schematic structure of a bilayer AGNR in (a) α alignment and (b) β alignment

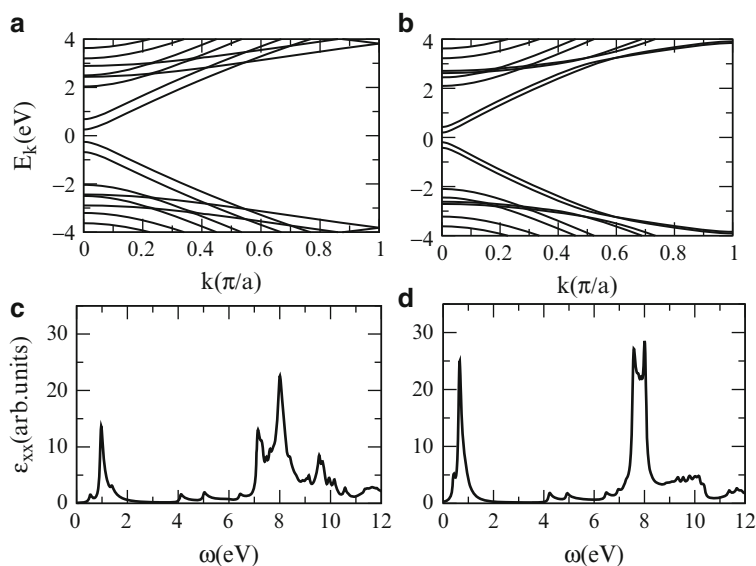


Fig. 6.15 Band structure of bilayer ANGR-8, obtained using the PPP-RHF method in (a) α alignment and (b) β alignment. Optical absorption spectra of the same ribbon in (c) α alignment and (d) β alignment

other so that their experimental measurement, coupled with our theoretical results, can possibly be used to determine the nature of alignment in multilayer ribbons. For a comprehensive discussion of the influence of edge alignment on the optical properties of multilayer AGNRs, we refer the reader to our recent work ([Gundra and Shukla 2011b](#)).

6.3.2.5 Electro-Absorption in Zigzag Graphene Nanoribbons

Electro-absorption (EA), which is nothing but the optical absorption in the presence of a static external electric field, is a commonly used probe of optical properties of materials and has been used extensively in the field of π -conjugated polymers ([Lies](#)

Fig. 6.16 Linear absorption spectrum (solid black line) and the electro-absorption spectrum (dotted red line) of ZGNR-10 in the presence of lateral electric field (E_y) of strength 0.2 V/\AA , calculated by the PPP-UHF method

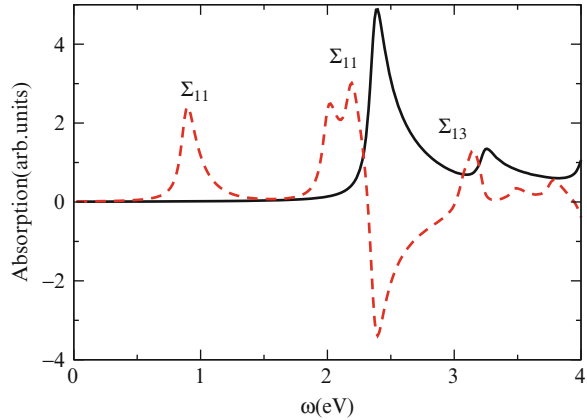
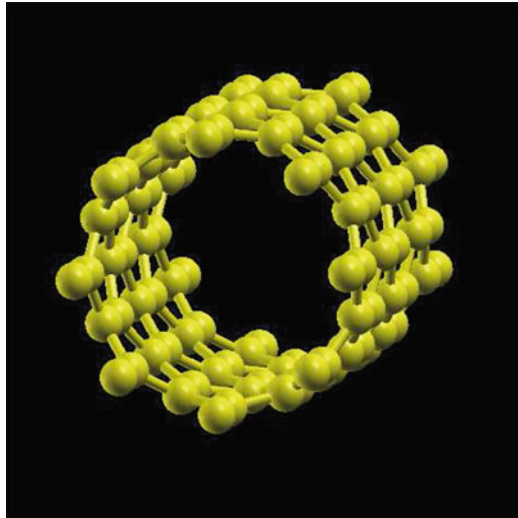
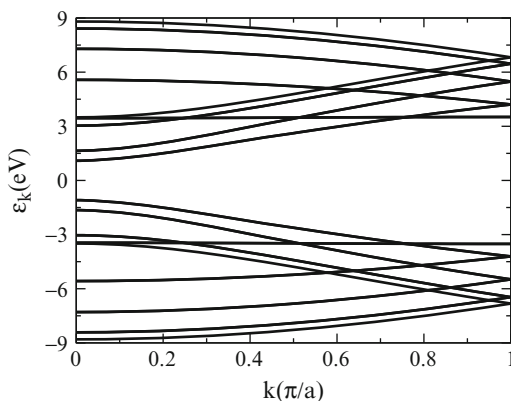


Fig. 6.17 The schematic structure of SWCNT (8,0). For brevity, carbon atoms belonging to the first three unit cells are displayed



et al. 1997). Quantitatively, it is defined as the difference of the optical absorption spectrum with, and without, an external static electric field. In a recent work (Gundra and Shukla 2011a), we argued that the EA spectroscopy provides a natural way of probing the electric-field-driven half-metallicity of ZGNRs. To illustrate this, we present the EA spectrum of ZGNR-10 in Fig. 6.16, calculated in the presence of a lateral external electric field of strength 0.2 V/\AA , using our PPP-UHF approach. The linear absorption spectrum of the ribbon without the external field, for its spin-polarized ground state, is also presented in the same figure. The electric-field-driven half-metallic nature of ZGNR-10 is clearly evident with the presence of two energetically split peaks, corresponding to two different Σ_{11} transitions, among the spin-up and spin-down electrons. Therefore, EA spectroscopy can serve as a useful optical probe to probe both the edge magnetism and related half-metallic nature of ZGNRs.

Fig. 6.18 Band structure of SWCNT (8,0), obtained using the PPP-RHF method

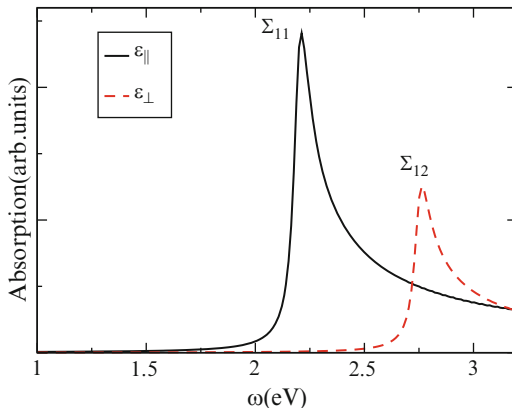


6.3.2.6 Band Structure and Optical Absorption Spectrum of Carbon Nanotubes

Single-walled carbon nanotubes (SWCNTs) exhibit excellent electronic properties and have been studied extensively over the last few decades (Dresselhaus et al. 2001). In this work, we present the band structure and optical properties of insulating SWCNT (8,0) obtained using PPP-RHF method. Even though the PPP model has been used by other authors to explore the electronic and optical properties of carbon nanotubes (Wang et al. 2006, 2007; Zhao and Mazumdar 2004, 2007; Zhao et al. 2006), the calculations are restricted to nanotubes of finite length, and periodic boundary conditions were not imposed. The schematic structure of SWCNT (8,0) is presented in Fig. 6.17. In these calculations, carbon-carbon nearest-neighbor distance was taken to be 1.42 \AA , and hopping was restricted to the nearest neighbors, with the hopping term $t = 2.4 \text{ eV}$. Similar to the case of GNRs, we have used the screened Coulomb parameters of Chandross and Mazumdar (1997), with $U = 8.0 \text{ eV}$ and $\kappa_{i,j} = 2.0$ ($i \neq j$) and $\kappa_{i,i} = 1$. Figure 6.18 displays the band structure of SWCNT (8,0) obtained using our approach. We note that the band structure of this SWCNT is similar to that of AGNRs, with a direct band gap of 2.18 eV at $k = 0$.

The optical absorption spectrum of SWCNT (8,0), computed using the PPP-RHF approach, is presented in Fig. 6.19. Due to the cylindrical symmetry of CNTs, their electric-dipole optical transitions are either through longitudinally polarized photons with polarization direction along the axis of the tube (x -direction), or the transversely polarized photons, with the polarization in the radial direction, in the yz plane. In Fig. 6.19, we denote the longitudinally polarized absorption spectrum as $\epsilon_{\parallel}(\omega)$ ($= \epsilon_{xx}(\omega)$), and the transverse one as $\epsilon_{\perp}(\omega)$ ($= \sqrt{\epsilon_{yy}(\omega)^2 + \epsilon_{zz}(\omega)^2}$, with $\epsilon_{yy}(\omega) = \epsilon_{zz}(\omega)$). While a detailed investigation of the optical absorption of SWCNTs will be published elsewhere, we note that the peaks corresponding to two types of polarizations are well separated in energy, and, therefore, can be identified in absorption experiments. The peak in $\epsilon_{\parallel}(\omega)$ corresponds to the Σ_{11} transition,

Fig. 6.19 Optical absorption spectrum of SWCNT (8,0), obtained by PPP-RHF method. The *solid black line* represents $\epsilon_{\parallel}(\omega)$, while the *dotted red line* denotes $\epsilon_{\perp}(\omega)$. A line width of 0.05 eV was assumed



located at the direct band gap (2.18 eV), while the peak in $\epsilon_{\perp}(\omega)$ at 2.77 eV denotes Σ_{12} transition. These results of ours on SWCNT (8,0) in the infinite length limit are in good quantitative agreement with the corresponding PPP-HF results reported by [Zhao and Mazumdar \(2004\)](#), based upon finite fragment calculations.

6.4 Conclusions and Future Directions

In this chapter, we have applied a PPP model Hamiltonian-based approach to study the electronic structure and optical properties of finite, as well as 1D periodic, graphene nanostructures such as fullerene C_{60} , graphene nanodisks, graphene nanoribbons, and single-wall carbon nanotubes. In case of periodic systems, calculations were performed at the mean-field Hartree-Fock level, whereas for the finite systems, we went beyond the mean field and included the electron-correlation effects at the SCI level. We computed the linear optical absorption spectrum of fullerene C_{60} , and the results obtained with screened Coulomb parameters were found to be in good agreement with the experiments. We also probed the optical absorption in graphene nanodisks using our approach and found that their shape, and the edge structure, influences their absorption spectrum considerably.

For 1D periodic systems, we computed the band structure and optical absorption spectra of monolayer GNRs of different geometries, and bilayer GNRs in Bernal stacking, but with different edge alignments. We found that the band structure and optical absorption spectra of GNRs depend crucially on their geometrical parameters, thereby allowing the possibility of an all-optical determination of the nature of their edge termination, as well as number and alignment of different layers for multilayer GNRs. We also demonstrated the sensitivity of the optical absorption spectrum of the ZGNRs to the nature of their edge-magnetized ground state and argued that their EA spectrum provides an efficient way of probing their electric-field-driven half-metallicity. Furthermore, for the first time, we applied our

PPP-model-based approach to compute the band structure and optical absorption spectrum of an insulating SWCNT in the infinite periodic limit.

It is quite remarkable that the PPP model, which was originally developed to describe the electronic structure of π -conjugated molecules and polymers, also can be applied successfully to describe the physics of other π -electron systems such as graphene nanostructures, as also the curved systems such as fullerenes and carbon nanotubes, for which the σ – π separation is no longer valid. In the future we aim to extend our PPP model-based preliminary calculations on fullerene C₆₀, and graphene nanodisks, by performing higher-level CI calculations employing approaches such as the MRSDCI method to study their optical properties and low-lying excited states. For the case of 1D periodic systems such as GNRs and CNTs, we intend to include the influence of electron correlation effects on their band structure. Furthermore, we also plan to incorporate the excitonic effects in the optical absorption spectra of these systems. It will also be of interest to extend this PPP-model-based approach to study multi-wall CNTs, as well as higher-dimensional systems such as graphene, and graphite. The work along these directions is currently under way in our group, and the results will be presented in future publications.

Acknowledgements We thank the Department of Science and Technology (DST), Government of India, for providing financial support for this work under Grant No. SR/S2/CMP-13/2006. K. G. is grateful to Dr. S. V. G. Menon for his continued support of this work.

References

- Ajje H, Alvarez MM, Anz SJ, Beck RD, Diedrich F, Fostiropoulos K, Huffman DR, Krätschmer W, Rubin Y, Shriver KE, Sensharma D, Whetten RL (1990) *J Phys Chem* 94:8630
- André JM, Vercauteren DP, Bodart VP, Fripiat JG (1984) *J Comp Chem* 5:535
- Barford W (2005) *Electronic and optical properties of conjugated polymers*. Clarendon Press, Oxford
- Barieswyl D, Campbell DK, Mazumdar S (1992) In: Keiss H (ed) *Conjugated conducting polymers*. Springer-Verlag, Berlin
- Barone V, Hod O, Scuseria GE (2006). *Nano Letts* 6:2748
- Bursill RJ, Barford W (2009) *J Chem Phys* 130:234302
- Castro EV, Novoselov KS, Morozov SV, Peres NMR, dos Santos JMBL, Nilsson J, Guinea F, Castro AH (2007) *Phys Rev Lett* 99:216802
- Chandross M, Mazumdar S (1997) *Phys Rev B* 55:1497
- Dresselhaus MS, Dresselhaus G, Avouris P (2001) *Carbon nanotubes: synthesis, structure, properties, and applications*, Vol 80. *Topics in applied physics*. Springer, Berlin
- Ezawa M (2006) *Phys Rev B* 73:045432
- Ezawa M (2008) *Physica E* 40:1421
- Fernández-Rossier J, Palacios JJ (2007) *Phys Rev Lett* 99:177204
- Gasyňa Z, Schatz PN, Hare JP, Dennis TJ, Kroto HW, Taylor R, Walton DRM (1991) *Chem Phys Lett* 183:283
- Güçlü AD, Potasz P, Voznyy O, Korkusinski M, Hawrylak P (2009) *Phys Rev Lett* 103:246805
- Geim AK, Novoselov KS (2007) *Nat Mat* 6:183
- Ghosh H, Shukla A, Mazumdar S (2000) *Phys Rev B* 62:12763

- Greer JC (2000) *Chem Phys Lett* 326:1567
- Gundra K, Shukla A (2011a) *Phys Rev B* 83:075413
- Gundra K, Shukla A (2011b) *Phys Rev B* 84:075442
- Gundra K, Shukla A (2012) *Comp Phys Comm* 183:677
- Han MY, Ozyilmaz B, Zhang YB, Kim P (2007) *Phys Rev Lett* 98:206805
- Harigaya K, Abe S (1994) *Phys Rev B* 49:16746
- Hod O, Barone V, Scuseria GE (2008) *Phys Rev B* 77:035411
- Iijima S (1991) *Nature* 354:56
- Jug K (1990) *Int J Quant Chem* 37:403
- Jung J, MacDonald AH (2009) *Phys Rev B* 79:235433
- Kan EJ, Li Z, Yang J, Hou JG (2007) *Appl Phys Lett* 91:243116
- Kertesz M (1982) *Adv Quant Chem* 15:161
- Kim J, Su WP (1994) *Phys Rev B* 50:8832
- Kinza M, Orloff J, Honerkamp C (2010) *Phys Rev B* 82:155430
- Kroto HW, Heath JR, O'Brien SC, Curl RF, Smalley RE (1985) *Nature* 318:162
- László L, Udvardi L (1987) *Chem Phys Lett* 136:418
- László L, Udvardi L (1989) *J Mol Struct (Theochem)* 183:271
- Leach S, Vervloet M, Després A, Bréheret E, Hare JP, Dennis TJ, Kroto HW, Taylor R, Walton DRM (1992) *Chem Phys* 160:451
- Lee M, Song OK, Seo JC, Kim D, Suh YD, Jin SM, Kim SK (1992) *Chem Phys Lett* 196:325
- Lies M, Jeglinski S, Vardeny ZV, Ozaki M, Yoshino K, Ding Y, Barton T (1997) *Phys Rev B* 56:15712
- Fujita M, Wakabayashi K, Nakada K, Kusakabe K (1996) *J Phys Soc Jpn* 65:1920
- Malliaras G, Friend R (2005) *Phys Today* 58:53
- Mataga N, Nishimoto K (1957) *Z Physik Chemie* 12:140
- Nakada K, Fujita M, Dresselhaus G, Dresselhaus MS (1996) *Phys Rev B* 54:17954
- Neto AHC, Guinea F, Peres NMR, Novoselov K, Geim AK (2009) *Rev Mod Phys* 81:109
- Novoselov KS, Geim AK, Morozov SV, Jiang D, Zhang Y, Dubonos SV, Grigorieva IV, Firsov AA (2004) *Science* 306:666
- Ohno K (1964) *Theor Chim Acta* 2:219
- Palacios JJ, Rossier JF, Brey L, Fertig HA (2010) *Semicond Sci Tech* 25:033003
- Pariser R, Parr RG (1953) *Trans Faraday Soc* 49:1275
- Parr RG (1952) *J Chem Phys* 20:239
- Pisani C, Dovesi R (1980) *Int J Quant Chem* 17:501
- Prezzi D, Varsano D, Ruini A, Marini A, Molinari E (2008) *Phys Rev B* 77:041404
- Psiachos D, Mazumdar S (2009) *Phys Rev B* 79:155106
- Raghu C, Pati YA, Ramasesha S (2002) *Phys Rev B* 66:035116
- Ren SL, Wang Y, Rao AM, McRae E, Holden JM, Hager T, Wang K, Lee WT, Ni HF, Selegue J, Eklund P (1991) *Appl Phys Lett* 59:2678
- Ridder KA, Lyding JW (2009) *Nat Mat* 8:235
- Ruiz A, Bretón J, Liorente JMG (2001) *J Chem Phys* 114:1272
- Ruiz A, Hernández-Rojas J, Bretón J, Liorente JMG (1998) *J Chem Phys* 109:3573
- Salem L (1966) *The molecular orbital theory of conjugated systems*. W. A. Benjamin, Inc., New York
- Schulten K, Ohmine I, Karplus M (1975) *J Chem Phys* 64:4422
- Schumacher S (2011) *Phys Rev B* 83:081417(R)
- Shukla A (2002) *Phys Rev B* 65:125204
- Shukla A (2004a) *Chem Phys* 300:177
- Shukla A (2004b) *Phys Rev B* 69:165218
- Shukla A, Dolg M, Stoll H (1998) *Phys Rev B* 58:4325
- Shukla A, Dolg M, Stoll H, Fulde P (1996) *Chem Phys Lett* 262:213
- Shukla A, Dolg M, Stoll H, Fulde P (1999) *Phys Rev B* 60:5211
- Shukla A, Ghosh H, Mazumdar S (2001) *Synth Met* 116:87
- Shukla A, Ghosh H, Mazumdar S (2003) *Phys Rev B* 67:245203

- Shukla A, Ghosh H, Mazumdar S (2004) Synth Met 141:59
Shukla A, Mazumdar S (1999) Phys Rev Lett 83:3944
Son YW, Cohen ML, Louie SG (2006a) Phys Rev Lett 97:216803
Son YW, Cohen ML, Louie SG (2006b) Nature 444:347
Sony P, Shukla A (2005a) Phys Rev B 71:165204
Sony P, Shukla A (2005b) Synth Met 155:368
Sony P, Shukla A (2005c) Synth Met 155:316
Sony P, Shukla A (2007) Phys Rev B 75:155208
Sony P, Shukla A (2009) J Chem Phys 131:014302
Sony P, Shukla A (2010) Comp Phys Comm 181:821
Soos ZG, Ramasesha S, Galvao DS (1993) Phys Rev Lett 71:1609
Voronov GS (2007) Phys Rev Lett 99:177204
Andreoni W (2000) Physics of fullerene-based and fullerene-related materials. Kluwer Academic, Dordrecht
Wang WL, Meng S, Kaxiras E (2008) Nano Lett 8:241
Wang WL, Yazyev OV, Meng S, Kaxiras E (2009) Phys Rev Lett 101:157201
Wang Z, Zhao H, Mazumdar S (2006) Phys Rev B 74:195406
Wang Z, Zhao H, Mazumdar S (2007) Phys Rev B 76:115431
Yamashiro A, Shimoi Y, Harigaya K, Wakabayashi K (2003) Phys Rev B 68:193410
Yang L, Cohen ML, Louie SG (2007a) Nano Lett 7:3112
Yang L, Cohen ML, Louie SG (2008) Phys Rev Lett 101:186401
Yang L, Park CH, Son YW, Cohen ML, Louie SG (2007b) Phys Rev Lett 99:86801
Yazyev O (2010) Rep Prog Phys 73:056501
Yazyev OV (2008) Phys Rev Lett 101:037203
Ye A, Shuai Z, Bredas JL (2003) Phys Rev B 65:045208
Zhao H, Mazumdar S (2004) Phys Rev Lett 93:157402
Zhao H, Mazumdar S (2007) Phys Rev Lett 98:166805
Zhao H, Mazumdar S, Sheng CX, Tong M, Vardeny ZV (2006) Phys Rev B 73:075403